SUPPLEMENTARY INFORMATION

I. Linear transmission properties of the sample

The transmission of the 1.3-mm photonic crystal (PhC) waveguide is illustrated in Figure S1. Total insertion loss (before and after coupling optics) is estimated to be 8 dB at 1544 nm (group index n_g = 6.9), including 4 dB directly attributable to the coupling optics. Carefully designed integrated mode-adapters reduce waveguide coupling losses to 1.5 dB/facet (insertion and exit) and suppress Fabry-Perot oscillations from facet reflections [S1]. The linear loss is α = 1 dB/mm at 1544 nm, scaled with n_g^2 [S2, S3]. The 3-dB optical transmission band extends between 1530 nm and 1560 nm and is bounded by the onset of the higher order odd mode and the even-mode cut off. At 1551 nm, the group velocity dispersion-to-loss ratio (β_2 ~ - 0.91 ps^2/mm; α ~ 1.1 dB/mm) is approximately -0.82 ps^2/dB.

The energy coupled into the PhC is estimated in the following way. We assume symmetric coupling loss (input and output) except for a factor accounting of mode mismatch on the input side (fiber to waveguide) that we do not have at the output since P_{out} is measured with a power meter in free space. This enables us to calculate the factor between the measured average power at input (output) and the value of the average power at the beginning (end) of the waveguide. Pulse energy is obtained by dividing by the repetition ratio.
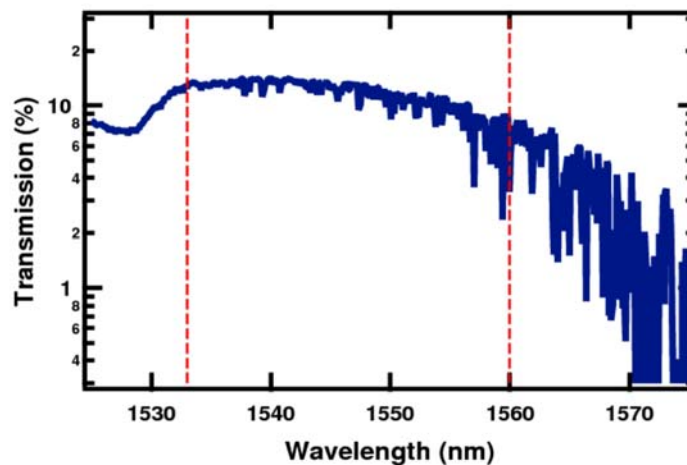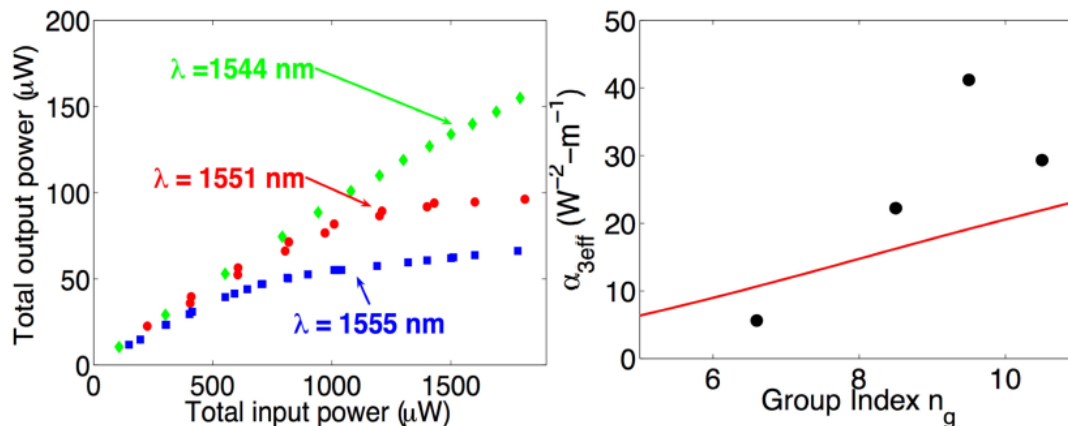

Figure S1 | Linear transmission of the PhC sample.

II. Nonlinear (three-photon) absorption of the PhC sample

The nonlinear absorption is revealed by output versus input power measurements as shown in Figure S2 (left). ThPA is negligible for lowest pulse energies in the experiment and begins to

have an impact at only the largest energies. This is apparent for the case of center pulse wavelengths of 1551 and 1555 nm. The abrupt saturation is reinforced by the compression effect. The wavelength-dependent effective nonlinear three-photon absorption (ThPA) parameters $a_{3eff} = a_f (n_g/n_0)^3$ in Figure S2 (right) are measured as in Ref. [S4].

Figure S2 | Nonlinear and input-output transmission characterization of the PhC sample. Left: Output versus input average power measured before (after) the coupling optics, i.e. objective-chip-objective values. Maximum power corresponds to about 20 pJ coupled energy per pulse. Right: Effective nonlinear absorption parameter a_{3eff} (points – experiment, line – theory).

III. Nonlinear Schrödinger equation (NLSE) and parameters

In addition to the main equation (1), the auxiliary carrier equation introduces a non-instantaneous response through the carrier lifetime τ_c: $\dfrac{\partial N_c}{\partial t} = \dfrac{\alpha_{3eff}}{3\hbar\omega A_{3eff}} |E|^6 - \dfrac{N_c}{\tau_c}$. The free-carrier dispersion coefficient δ includes n_g scaling: $\delta = -\dfrac{q^2}{2\omega^2 \varepsilon_o n_o m^*} \dfrac{n_g}{n_o}$. Parameters are obtained directly from experimental measurements or calculated as required [A_{eff}] and are reported in Table S1. The effective nonlinear parameters α_{3eff} and γ_{eff} were experimentally measured as in Ref. [S4]. The bulk Kerr $n_2 = 0.57\times10^{-17}$ m^2/W [S5] and $\alpha_3 = 2.5\times10^{-26}$ m^3-W^{-2} [S6] coefficients employed in the calculations are in agreement with well-known models, experimentally verified for the similar AlGaAs material [S7]. The values in Table S1 are calculated given the definitions $\gamma_{eff} = n_2 k_0 n_g^2 / A_{3eff}$ and $\alpha_{3eff} = \alpha_3 n_g^3 / A_{5eff}^2$, with the nonlinear effective areas defined in a similar way as

in Ref. [S8] as: $\dfrac{1}{A_{3eff}} = \dfrac{a \int\limits_{Cell} n^2 \kappa |\vec{E}|^4 \, dV}{\left(\int\limits_{Cell} n^2 |\vec{E}|^2 \, dV \right)^2}$ and $\dfrac{1}{A_{5eff}^2} = \dfrac{a^2 \int\limits_{Cell} n^3 \kappa |\vec{E}|^6 \, dV}{\left(\int\limits_{Cell} n^2 |\vec{E}|^2 \, dV \right)^3}$, with a the lattice period, $Cell$

meaning the volume of one waveguide period, n the refractive index and κ a function giving the ratio of the local value of nonlinear parameter to the value used in formula. Specifically, for the structure with holes, $\kappa = 1$ in the membrane and 0 outside. Moreover E is the vector electric field distribution of the waveguide Bloch modes derived via the planewave expansion method [S9]. Third-order nonlinear effects and linear propagation loss are taken to increase with n_g^2 [S2, S3, S10]. We assume $\sigma = 4 \times 10^{-21}(n_g/n_0)$ m^2 based on established data for GaAs lasers and scaled with the group index to correct for enhanced absorption.

**Table S1. Characteristic parameters of the GaInP PhCWG sample.**

λ (nm)[*]	1544	1551	1555	1559
group index n_g[*]	6.9	8.3	9.3	10.5
β_2 (ps^2-mm^{-1})[*]	-0.69	-0.91	-1.1	-1.3
β_3 (ps^3-mm^{-1})[*]	0.03	0.05	0.06	0.08
α_1 (cm^{-1})[+]	2.2	2.5	3.2	6
α_{3eff} (cm^{-1}-W^{-2})[†]	0.14	0.20	0.26	0.34
γ_{eff} (cm^{-1}-W^{-1})[†]	5.82	7.65	9.16	11.0
T_{FWHM} (ps)	3.77	3.25	2.85	2.47

[*] Measured   [†] Calculated   [+] Estimated

IV. Nonlinear Schrödinger equation (NLSE) simulation results

We solve the NLSE model employing an implicit Crank-Nicholson split-step method. In Figure S3 we demonstrate the simulated autocorrelation and accompanying spectra of the experimental data in Figure 2 of the manuscript. These simulations were conducted as outlined in the main paper. That is, all parameters are identical to experimental measurements, or calculated as required. No free parameters were allowed. One can see that both the autocorrelation and spectra correspond remarkably well given the complexity of the interaction between the various effects.

Importantly, the autocorrelation of 1551 nm reaches a minimum near 20 pJ, whereas the 1555 nm case shows a broader autocorrelation at these pulse energies, in agreement with the experimental observations.
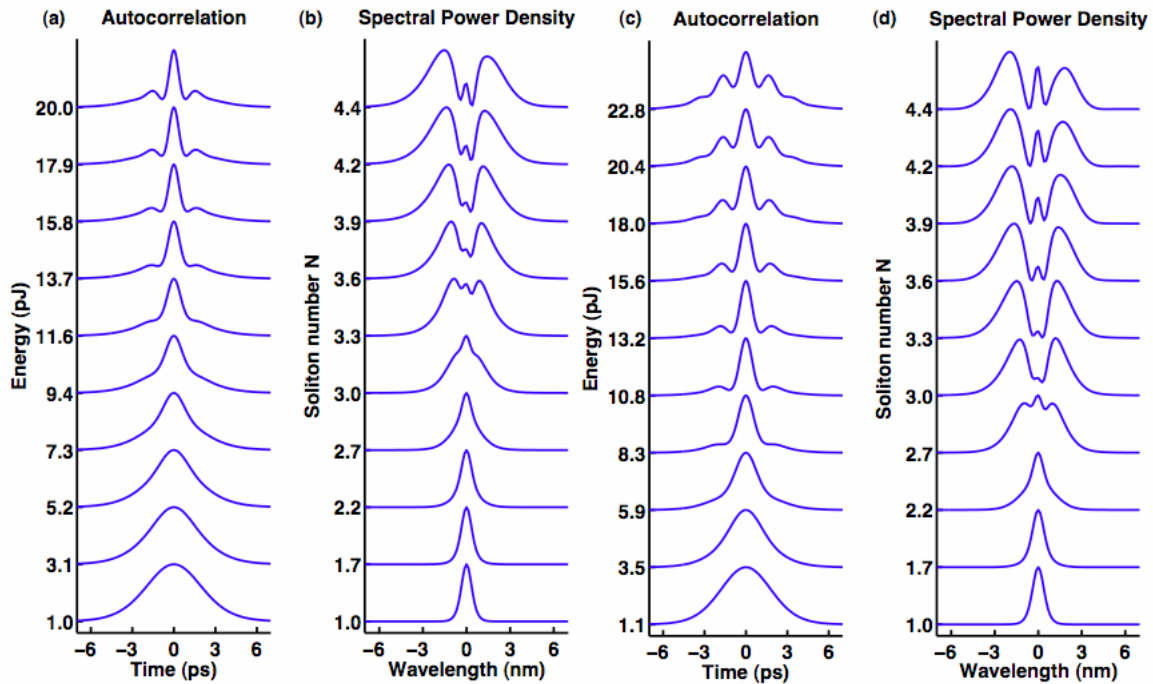
Figure S3 | Calculated spectra and autocorrelation traces corresponding to Figure 3. Intensity autocorrelation traces (**a** and **c**) of output pulses for increasing coupled pulse energies from 1.7 pJ to 22 pJ and corresponding spectra (**b** and **d**). **a** and **b**, Pulses centered at 1551 nm (n_g of 8.3). **c** and **d**, Pulses centered at 1555 nm (n_g of 9.3).

V. Limitations on soliton-effect compression due to three-photon absorption

In Figures S4 **a-e** we show the full simulations of the NLSE at various wavelengths and group indices, as detailed in the manuscript. All input powers are 20 pJ. Directly to the right, Figures S4 **f-j**, we show the equivalent case NLSE with suppressed three-photon absorption ($\alpha_3 = 0$) and suppressed free-carrier effects ($N_c = 0$) that would otherwise dominate at such large intensities. Third-order dispersion effects are considered, though they contribute negligibly.
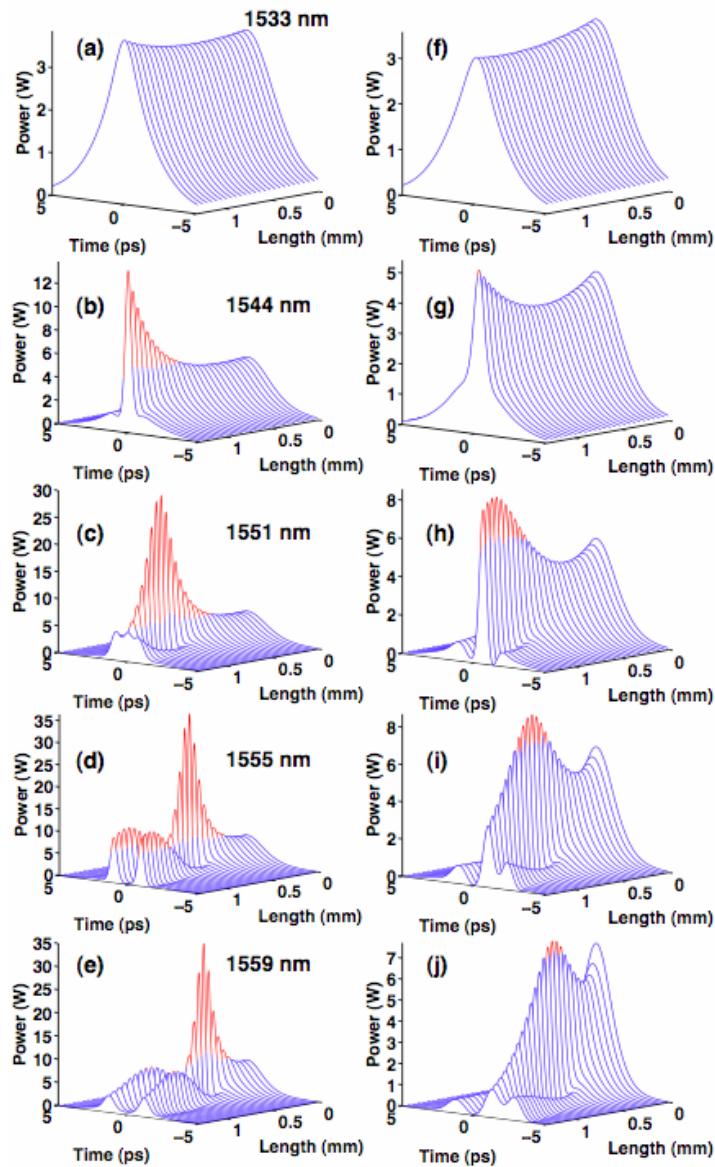
Figure S4 | Limitation of the soliton-effect pulse compression due to three-photon absorption. a-e, Simulated pulse propagation along the PhCWG at 1533, 1544, 1551, 1555, and 1559 nm with input energy 20 pJ, respectively. The red part of the curves corresponds to peak power values above the input peak power that are characteristic of pulse compression. **f-j,** Same as **a-e,** except with suppressed three-photon absorption ($\alpha_3 = 0$) and suppressed free-carrier effects ($N_c = 0$).

At 1533 nm, Figures S4 **a** and **f**, dispersion and nonlinear effects are extremely weak. Consequently the pulse changes negligibly over the sample length. The most striking effect of these simulations is that the peak powers are reduced from greater than 30 W with suppressed

effects to the 8 W observed experimentally for 1551 nm and 1555 nm. As discussed in the body of the paper, the main impact of the dissipative terms in the NLSE is to "slow" down the soliton dynamics, e.g. to increase the effective spatial scale as well as the effective soliton order, N, over which the soliton evolution is observed. This is readily seen by comparing Figures S4 **c** and **h**. In Figure S4 **h**, the pulse is maximally compressed at the sample output ($L = 1.3$ mm), whereas in Figure S4 **c**, the optimal sample length, z_{opt}, is observed at $L = 0.93$ mm. At 1559 nm ($n_g = 10.5$), the linear scattering losses dominate as mentioned in the paper [S2, S3], with a small contribution from nonlinear losses.

Materials limited by two-photon absorption would experience far greater attenuation, (e.g. have lower peak powers) and require much longer length scales to observe the same phenomena as they possess a greatly diminished critical intensity to trigger free-carrier effects [S11, S12]. Three-photon absorption thus places a fundamental limit to the peak power, and consequently the compression factor, that can be produced from this mechanism.

VI. Temporal soliton compression with tuned low group velocity dispersion photonic crystal waveguides.

The carefully control of group velocity dispersion [S11, S13, S14] in slow-light photonic crystal waveguides allows soliton compression to shorter pulse widths. Figure S5 below shows the modeled output and input pulse widths for β_2 values of 0.05, 0.10, and 0.20 ps^2/mm. The input pulse is 2 ps with 5 W peak power. The values employed in the simulation are identical to experimental parameters with the exception of modified β_2 values. As shown, with the suppressed two-photon absorption, pulse widths compressed down to 150 fs or less is possible on-chip.
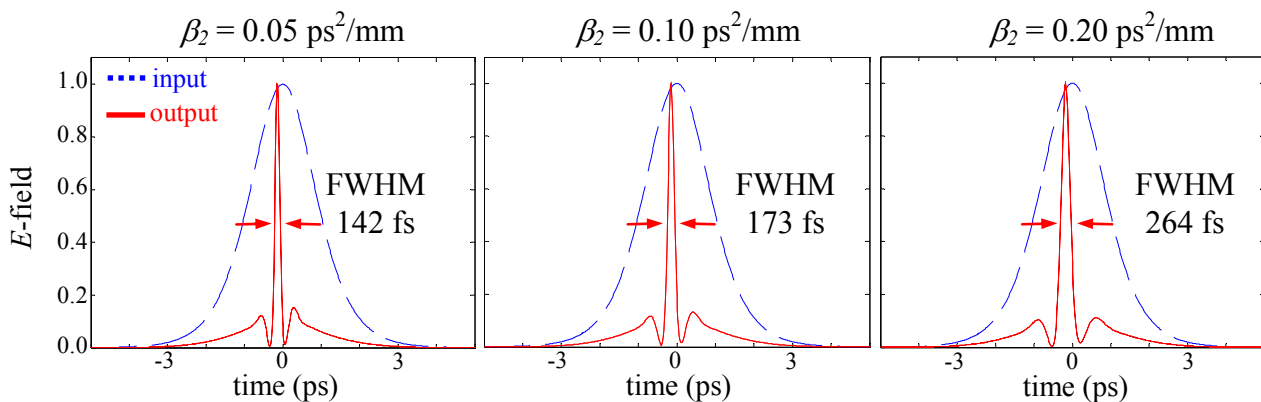

Figure S5 | Nonlinear Schrödinger equation numerical modeling of soliton compression down to 150 fs or shorter pulse widths. Modeled output (red solid) and input (blue dashed) pulse widths

for group velocity dispersion β_2 of 0.05, 0.10, and 0.20 ps^2/mm. The input pulsewidth is 2 ps with 5 W peak power.

VII. Towards integrated soliton-effects

Figure S6 shows the input pulse durations and energies employed in our series of experiments. The values are in Table 1 in the main paper. Note the input pulses are in the regime where they can be provided by current picosecond semiconductor laser diodes – instead of bulk femtosecond solid-state lasers – for soliton compression into femtosecond pulses. This extends the capabilities of picosecond laser diodes (with advantages such as compactness, direct electrical control and current applications in fluorescence lifetime spectroscopy for instance), allowing higher peak powers and finer temporal (probe) resolution. Note also that, in order to approach the $L/L_d \sim 1$ regime, nanowire channel waveguides require $\sim 100\times$ longer sample lengths (from the $\sim 100\times$ smaller β_2), which for the picosecond laser diodes regime, corresponds to tens of centimetres for each device length.
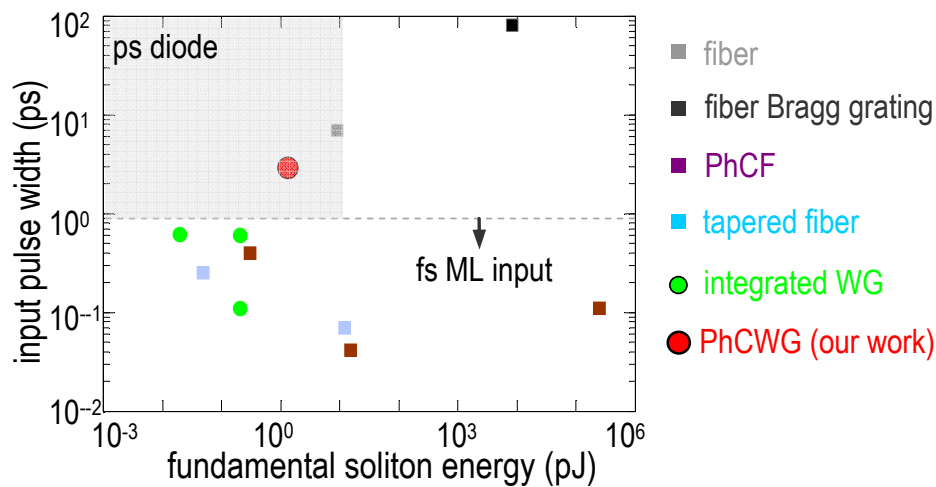
Figure S6 | Comparison of this work with previous leading efforts in the field of optical solitons effects. Experimentally measured input pulse widths vs. fundamental soliton energies in nanophotonic (circles) and fiber (squares) systems. The shaded (grey) region denotes the regime accessible with laser diodes, with minimum $\sim$ ps pulse widths and up to ~ 10 pJ pulse energies. The dash line denotes measurements with femtosecond mode-locked (ML) pulse inputs.

VIII. Von der Linde measurements of phase-noise

In Figure S7 we show measurements of the RF spectra from the soliton compression, where panel **a** shows the spectra after propagating through the sample and panel **b** shows the spectra from the mode-locked laser itself. The pulse energies used are ~ 20 pJ levels, which induces soliton compression in our samples. Figure S7 **c** shows the resulting von der Linde noise characterization [S15], which shows that there is no discernable difference in the optical pulse jitter before and after propagation in the photonic crystals, within the measurement accuracy. These measurements are described and summarized in the main manuscript.
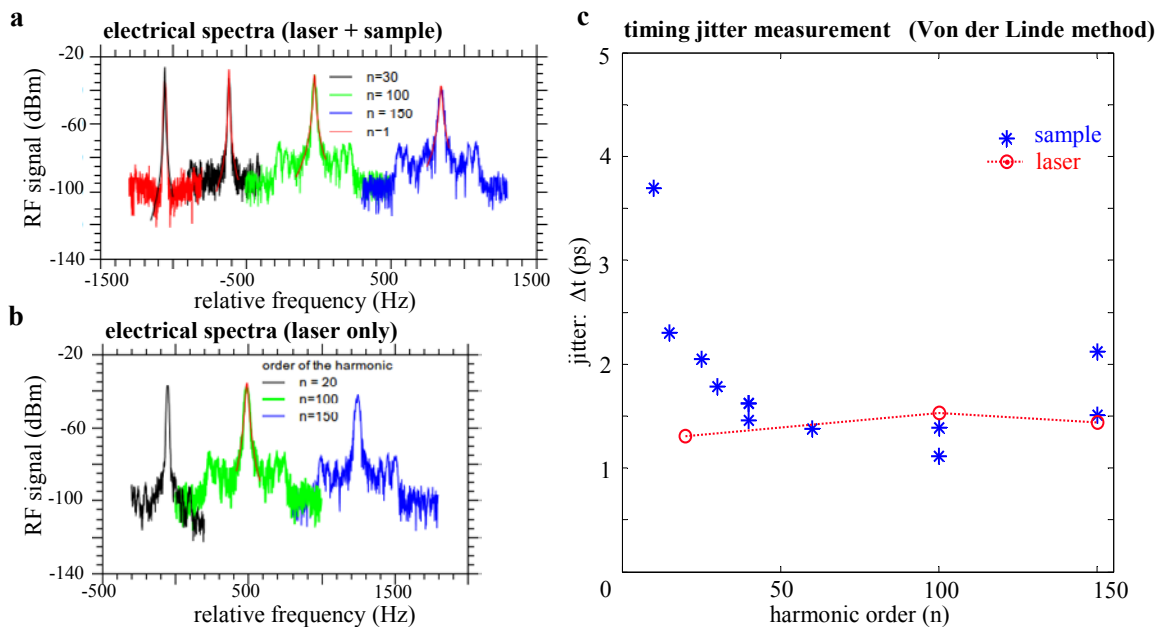
Figure S7 | RF spectra before and after soliton compression. a, Example RF spectra of the output optical solitons, after exiting the chip. **b,** Example RF spectra measured from the mode-locked fiber laser before entry into the photonic crystal chip. **c,** von der Linde phase noise characterization, illustrating the timing jitter for each harmonic. There is no discernable difference in the optical pulse jitter before and after propagation in the photonic crystal, within measurement accuracy. The jitter of the laser itself is ~ 4× larger than expected.

Supplementary References:

[S1] Tran, Q. V., Combrié, S., Colman, P. & De Rossi, A. Photonic crystal membrane waveguides with low insertion losses. *App. Phys. Lett.* **95**, 061105 (2009).

[S2] Hughes, S., Ramunno, L., Young, J. F. & Sipe, J. E. Extrinsic optical scattering loss in photonic crystal waveguides: Role of fabrication disorder and photon group velocity. *Phys. Rev. Lett.* **94**, 033903 (2005).

[S3] Engelen, R. J. P., Mori, D., Baba, T. & Kuipers, L. Two regimes of slow-light losses revealed by adiabatic reduction of group velocity. *Phys. Rev. Lett.* **101**, 103901 (2008).

[S4] Husko, C. *et al.* Non-trivial scaling of self-phase modulation and three-photon absorption in III-V photonic crystal waveguides. *Opt. Express* **17**, 22442–22451 (2009).

[S5] Sheik-Bahae, M., Hagan, D. J. & Van Stryland, E. W. Dispersion and band-gap scaling of the electronic Kerr effect in solids associated with two-photon absorption. *Phys. Rev. Lett.* **65**, 96–99 (1990).

[S6] Wherrett, B. S. Scaling rules for multiphoton interband absorption in semiconductors. *Opt. Soc. Am. B* **1**, 67–72 (1984).

[S7] Siviloglou, G. A. *et al.* Enhanced third-order nonlinear effects in optical AlGaAs nanowires. *Opt. Express* **14**, 9377–9384 (2006).

[S8] Bhat, N. A. R. & Sipe, J. E. Optical pulse propagation in nonlinear photonic crystals. *Phys. Rev. E* **64**, 056604 (2001).

[S9] Johnson, S. G. & Joannopoulos, J. Block-iterative frequency-domain methods for Maxwell's equations in a planewave basis. *Opt. Express* **8**, 173–190 (2001).

[S10] Soljačić, M. & Joannopoulos, J. D. Enhancement of nonlinear effects using photonic crystals. *Nature Mater.* **3**, 211–219 (2004).

[S11] Monat, C. *et al.* Slow light enhancement of nonlinear effects in silicon engineered photonic crystal waveguides. *Opt. Express* **17**, 2944–2953 (2009).

[S12] Baron, A. *et al.* Light localization induced enhancement of third order nonlinearities in a GaAs photonic crystal waveguide. *Opt. Express* **17**, 552–557 (2009).

[S13] Kubo, S., Mori, D. & Baba, T. Low-group-velocity and low-dispersion slow light in photonic crystal waveguides. *Opt. Lett.* **32**, 2981–2983 (2007).

[S14] Petrov, A. Y. & Eich, M. Zero dispersion at small group velocities in photonic crystal waveguides. *Appl. Phys. Lett.* **85**, 4866–4868 (2004).

[S15] Von der Linde, D. Characterization of the noise in continuously operating mode-locked lasers. *Appl. Phys. B* **39**, 201–217 (1986).